Koukouvinis, P., Naseri, H. & Gavaises, M. (2016). Performance of turbulence and cavitation models in prediction of incipient and developed cavitation. International Journal of Engine Research, doi: 10.1177/1468087416658604

Performance of Turbulence and Cavitation Models in Prediction of Incipient and Developed Cavitation

Koukouvinis Phoevos*, Naseri Homa and Gavaises Manolis

School of Mathematics, Computer Science & Engineering, City University London

E-mail: Foivos.Koukouvinis.1@city.ac.uk

Abstract. The aim of the current paper is to assess the impact of turbulence and cavitation models on the prediction of Diesel injector nozzle flow. Two nozzles are examined, an enlarged one, operating at incipient cavitation and an industrial injector tip operating at developed cavitation. The turbulence model employed include the RNG k-ε, Realizable k-ε and k-omega SST RANS models, linear pressure-strain Reynolds Stress Model and the WALE Large Eddy Simulation model. The results indicate that all RANS and the Reynolds stresses turbulence models have failed to predict cavitation inception, due to their limitation to resolve adequately the low pressure existing inside vortex cores, which is responsible for cavitation development in this particular flow configuration. Moreover, RANS models failed to predict unsteady cavitation phenomena in the industrial injector. On the other hand, the WALE LES model was able to predict incipient and developed cavitation, while also capturing the shear layer instability, vortex shedding and cavitating vortex formation. Furthermore, the performance of two cavitation methodologies is discussed within the LES framework. In particular, a barotropic model and a mixture model based on the asymptotic Rayleigh-Plesset equation of bubble dynamics have been tested. The results indicate that although the solved equations and phase change formulation is different in these models, the predicted cavitation and flow field were very similar at incipient cavitation conditions. At developed cavitation conditions standard cavitation models may predict unrealistically high liquid tension, so modifications may be essential. It is also concluded that accurate turbulence representation is crucial for cavitation in nozzle flows.

Keywords: Cavitation, RANS, LES, cavity shedding, step nozzle, Diesel injector

1. Introduction

Inception and development of cavitation is a two-way interaction problem between the formed bubbles and the flow. This interaction is enhanced by the fact that most practical flows are turbulent; under such flow conditions the scales of fluid motion underlying in the flow field in the form of vortices can contribute and even become the dominant mechanism causing cavitation formation, leading to structures termed as cavitating vortices[1]. Cavitating vortices are common in engineering applications and can exist in propeller blade tip and surfaces, injectors, and pumps. They can significantly affect the flow field characteristics and cause substantial reduction in efficiency and increase erosion. Vortex or string-type cavitation has been observed in studies of in-nozzle flow of Diesel injectors; vortices initiate from the transient flow inside the sac volume and can induce significant hole to hole variations [2, 3]. Formation of vapour in the core of vortices is an additional mechanism for generation of vorticity, hence it modifies the dynamics of turbulence[4]. Production of vorticity is due to variations in the density which are not aligned with pressure variations and create a baroclinic torque[5]. Experimental studies on stationary hydrofoils shows that baroclinic torques contribute to vorticity generation especially at regions of cavity collapse [6]. Investigation of vorticity generation transport equation shows that vortex stretching, dilatation and baroclinic torque due to density gradients in cavitating flows are major sources of vorticity generation [7]. Cavitating vortices are especially important in erosion studies since they can be very aggressive and cause significant damage as they collapse[1]. Erosive vortex rings have been used in industrial applications for cutting rock and underwater cleaning. Numerical comparison of erosive power of a cavitating vortex ring and a spherical bubble indicate that the collapse of cavitating bubble ring should be more erosive than the collapse of a spherical bubble [8]. Vortices are also formed in the shear layer, for example in turbulent wake of bluff bodies, mixing layers of liquid jets or between the recirculation region and bulk flow in separated flows. In a forward-facing-step nozzle, as the flow enters the nozzle and accelerates it separates from the edge, forming a

recirculation region at the entrance. The velocity in the recirculation region is lower than the velocity of the bulk flow in the nozzle, hence a shearing layer is formed. These vortices can cavitate and they constantly pair-up forming larger vortices downstream. Shear layer vortices can have small length and time scales and contribute to viscous dissipation [9]. Prediction of this coherent structures of shear flow requires resolving the flowfield down to the inertial subrange.

Interaction of turbulence and cavitation has been studied both experimentally and numerically by many researchers on various application fields. In a study with a sharp edged plate in a cavitation channel, Fluorescent Particle Image Velocimetry (PIV) is used to assess the effect of cavitation on shear layer instabilities and flow turbulence downstream the shear layer [10]. The two-way interaction between cavitation and turbulence was investigated with Direct Numerical Simulation (DNS) with main interest on the development of shear layer instabilities [11]. It is reported that turbulence is modulated by cavitation. This modulation can form a basis for a Sub Grid Scale (SGS) model for cavitation in Large Eddy Simulation (LES). Reynolds Averaged Navier-Stokes (RANS) models are computationally less expensive than LES but they can have significant shortcomings in modelling turbulent cavitating flows. It has been shown that traditional RANS/URANS models may overestimate turbulent viscosity in cavitation zones, preventing the development of a re-entrant jet motion and the cavity shedding pattern, yielding unnatural results [12-14]. Eventually, a correction [15] has been applied in order to modify the turbulent kinetic energy term in the two equation model closure by reducing the eddy viscosity in mixture regions and with this term it was possible to replicate the observed experimental shedding pattern. The divergence of the velocity fluctuations is not zero in mixture transport equations of RANS models and additional dissipation terms appear [16]. Without including the extra dissipation terms, namely the mixture pressure dilatation, mixture turbulent mass flux and the compressible dissipation, a stable cavity without recirculation and shedding is predicted. By adding the dissipation due to mixture compressibility, the re-entrant jet motion is predicted which results in predicting the cyclic behaviour of cavitation. Other approaches to predict turbulent unsteadiness in

78 cavitating flows include limiting the eddy viscosity by applying a filter-based modification to k-ε
79 model[17] or adding a scale-adaptive term to transport equation of the turbulent length scale in k− ℓ
80 turbulence model[18]. Other researchers [3, 19, 20] have tried to compensate for the turbulent effect on
81 cavitation inception through the inclusion of an additional semi-empirical pressure fluctuation term to
82 the saturation pressure. The importance of accurately capturing the turbulence induced pressure
83 fluctuations in cavitating flows is highlighted in a study by Edelbauer et al.[21], with main focus on
84 throttles and constrictions appearing in fuel injection systems. They have compared RANS and LES
85 simulations of a cavitating throttle flow; even though they have employed a rather specialized variant
86 of the v^2-f turbulence model, they were unable to get good results in all cases examined, showing the
87 situational applicability of the RANS model. They conclude that RANS can predict cavitation with a
88 reasonably acceptable accuracy in an operating condition with high pressure difference, whereas it
89 fails to predict the cavitation at a lower pressure difference. It is worth mentioning the recent work of
90 Örley et al. [22], who employed an LES framework with cut-cell immersed boundary method and a
91 barotropic fluid, including the effect of non-condensable gas, for the simulation of a 9-hole Diesel
92 injector to obtain time resolved information on cavitating/turbulent flow structures in the injector sac,
93 orifices and jets.

94 The aim of the present work is to examine the influence of various turbulence models, including some
95 common RANS models e.g. k-ε, k-ω, RSM, as well as some of their modifications that have been
96 proposed for the compensation of mixture compressibility effects, such as the Reboud et al. correction
97 [15]. The application is on a square throttle with a sudden constriction which has been examined in the
98 past both experimentally and numerically [23]; this configuration bears resemblance to the constrictions
99 inside injector passages. The results indicate that traditional turbulence models and even their
100 modifications fail to predict the incipient cavitation formation due to shear layer instabilities. Further
101 application in the flow of a Diesel injector tip suggests that while RANS models predict cavitation
102 formation, the formed cavity may be unphysically stable, especially when hole tapering is present.

However, more advanced turbulence models, such as Wall Adapting Local Eddy-viscosity[24] (WALE) LES are found to capture cavitation inception and development. Cavitation effects have been be modelled using a mixture model, where phase change is governed by the Schnerr and Sauer [25] and Zwart et al. [26] models. In addition, a new formulation of a Homogenous Equilibrium Model (HEM), similar to that developed by Schmidt [27], has been utilized.

2. Mathematical modelling of turbulence and cavitation

In this section, a brief description of the mathematical background of the involved models will be described, both regarding turbulence models and cavitation modelling. All the relevant models discussed have been employed using the ANSYS Fluent v15 software, either in the form of pre-existing models, or as programmed modifications through User Defined Functions (UDFs).

Since high accuracy is necessary to resolve fine features of flow, such as the vortex interaction with cavitation, second order schemes have been used for resolving the momentum equations, in case of RANS models. For the WALE LES model, a blended central/second order upwind scheme has been used for the momentum equation, since it is a good compromise between stability and low numerical diffusion. The density field was discretized with a second order upwind scheme, whereas the phase field in the 2-phase model was discretized with the Quadratic Upstream Interpolation for Convective Kinetics (QUICK) scheme in order to capture the high density ratios. Time advancement is done with a second order implicit method (three time level predictor-corrector, or midpoint method), to maintain accuracy and remove any time stepping stability constraints.

2.1. Turbulence modelling

Turbulence is an effect associated with chaotic and unsteady nature of fluid motion at high Reynolds numbers; indeed at such cases a complicated flow pattern emerges with many temporal and spatial scales of fluid motion, manifested as vortices through which an energy transfer occurs, from the largest scales of fluid motion to the smallest scales, where energy is dissipated due to viscous effects

[28]. The fundamental problem with turbulence is the fact that DNS of all scales is impossible for most industrial flows. The alternative is to emulate the effect of the energy transfer process with a proper model. This has the advantage that it is no longer required to take into account all relevant scales of fluid motion, but rather consider only the largest ones, depending on the model used. For example, RANS models focus only on the mean flow properties, whereas Large Eddy Simulation models include also the effect of the larger eddies which are anisotropic and model only the smallest ones; this fact forces the simulation in the latter option to be always in 3D and transient.

In the current work several well-known RANS models have been employed. These are the RNG k-ε, Realizable k-ε, SST k-ω and Reynolds Stress models. Some brief characteristics of these models are given below and the interested reader is addressed to a CFD handbook reference for more information, e.g. [28-30]:

- The k-ε model family is a 2-equation turbulence model, where the turbulent kinetic energy (k) and the turbulence dissipation (ε) are modelled using transport equations with diffusion and source terms calibrated from experiments. It is one of the most widely used models in industrial cases. Its main deficiency is the overestimation of turbulence production at stagnation points and underestimation of separation in adverse pressure gradients. Over time, modifications as the RNG and Realizable k-ε models have been developed to improve the accuracy of the model.

- The k-ω model family is a 2-equation turbulence model as well, which solves for turbulent kinetic energy (k) and specific dissipation rate (ω); this gives several advantages in respect to the k-ε model in predicting near wall regions accurately, due to the nature of the ω-equation in respect to the ε-equation. However, the standard k-ω model is somewhat sensitive to the boundary conditions of the specific dissipation rate. For that reason, the k-ω Shear Stress Transport (SST) model was developed, which is a blend between the k-ε and k-ω models, offering the best of both models.

- The linear strain pressure-strain Reynolds Stress Model (RSM), based on the work of Launder[31], is a more advanced version of the RANS models, which no longer assumes isotropy of the Reynolds stresses; contrary, one equation for each Reynolds stress term is solved, in addition to the turbulence dissipation. Eventually this leads to seven additional equations for 3D, which adds to a significant computational cost, but potentially it is the most general of the RANS models.

Additionally to the aforementioned models, the Reboud et al. modification [15] shall be examined; this modification aims to compensate the effect of the mixture compressibility in the vapour/liquid mixture region [32]. In general, the correction is applied during the calculation turbulent viscosity, where density ρ is replaced with a function f(ρ), as follows:

$$f(\rho) = \rho_V + (1-\alpha)^n (\rho_L - \rho_V) \quad (1)$$

where ρ is density, V and L indexes correspond to saturated vapour and liquid density respectively and n is an exponent the takes values ~10.

Eventually turbulent viscosity has the form [12]:

$$\mu_t = C_\mu f(\rho) \frac{k^2}{\varepsilon} \quad (2)$$

for the RNG k-ε model, or for the k-ω SST model:

$$\mu_t = f(\rho) \frac{a_1 k}{\max(a_1 \omega, S F_2)} \quad (3)$$

where C_μ = 0.845, a_1=5/9, $S = \sqrt{2S_{ij} : S_{ij}}$ with S_{ij} the components of the rate of strain tensor and F_2 a blending function [30]. These corrections are relevant only in unsteady simulations (URANS). Moreover, when compressible flow is involved, such as in the Diesel injector or the barotropic HEM model, an additional turbulence dissipation term is included in the turbulent kinetic energy equation, based on the modification of Sarkar et al.[33].

Apart from the aforementioned RANS models, the Wall Adapting Local Eddy-viscosity (WALE) model has been employed for the LES runs, since it is known that it performs significantly better in the near wall region in respect to the basic Smagorinsky LES model [24].

2.2. Cavitation modelling: the barotropic Homogenous Equilibrium Model (HEM)

For the homogenous equilibrium model, additional phase field variables are not needed, since the mass transfer occurs instantaneously, linking pressure to density only. So, one needs an appropriate equation of state (EOS) that corresponds to the phase change of the liquid to the liquid/vapour mixture.

In this work, for simplicity the influence of thermal effects have been omitted and a barotropic EOS is constructed as follows:

- the Tait EOS is used for the liquid, i.e. when $\rho \geq \rho_l$

- the isentropic gas EOS is used for the gas, i.e. when $\rho_v > \rho$

- for the mixture ($\rho_l > \rho \geq \rho_v$), the EOS is based on the Wallis speed of sound formula [34]:

$$\frac{1}{c_m^2 \rho_m} = \frac{a_l}{c_l^2 \rho_l} + \frac{a_v}{c_v^2 \rho_v} \tag{4}$$

where a corresponds to volume fraction, c to the speed of sound, ρ to the density and l and v indexes to liquid and vapour respectively. Considering that, for an isentropic fluid the speed of sound is [35]:

$$c^2 = \left(\frac{\partial p}{\partial \rho} \right)_s \tag{5}$$

it is possible to integrate eq. 5 in respect to the mixture density and obtain pressure (see also appendix A). Eventually, the complete equation of state is the following, see also an indicative graph of the EOS at Figure 1:

$$p(\rho)=\begin{cases} B\left[\left(\frac{\rho}{\rho_l}\right)^n-1\right]+p_{sat,L} & \rho \geq \rho_l \\ \frac{c_v^{\,2}c_l^{\,2}\rho_l\rho_v(\rho_v-\rho_l)}{c_v^{\,2}\rho_v^{\,2}-c_l^{\,2}\rho_l^{\,2}}\ln\left(\frac{\rho}{c_l^{\,2}\rho_l(\rho_l-\rho)+c_v^{\,2}\rho_v(\rho-\rho_v)}\right)+p_{ref} & \rho_l \geq \rho > \rho_v \\ C\rho^{\gamma} & \rho_v > \rho \end{cases} \quad (6)$$

The factor B corresponds to the bulk modulus of the liquid, n is an exponent determining the stiffness of the Tait equation of state, which is commonly set to 7.15 for weakly compressible liquids [36], C is the constant of the isentropic process and γ is the heat capacity ratio. In the above equation p_{ref} and $p_{sat,L}$ are reference values in order to make sure that the pressure is a continuous function of density, thus $\lim_{\rho\to\rho_v^+} p(\rho)=\lim_{\rho\to\rho_v^-} p(\rho)$ and $\lim_{\rho\to\rho_l^+} p(\rho)=\lim_{\rho\to\rho_l^-} p(\rho)$. It becomes obvious from the formulation of the equation, that during the phase change there is a small pressure difference equal to $\Delta p= p_{sat,L} - p_{sat,V}$. In practice, this difference is small in comparison with the pressure levels involved in the simulation, e.g. for the present case, the difference is around 4500Pa, whereas the pressure level in the current simulation is of the order of ~2bar. Moreover, while it is true that the equation of state is not perfectly accurate for the sharp change of pressure in the saturation dome, it has the advantage of having a continuous speed of sound, which helps achieving convergence with the pressure-based solver utilized. The values used in this study are shown in Table I.

Table I. Thermodynamic properties for water/vapour with the barotropic HEM, values have been selected an saturation properties of water/steam at 20°C [37].

Liquid properties		
B	$307.1\cdot10^6$	Pa
n	7.15	(-)
$\rho_{sat,L}$	998.16	kg/m^3
$c_{sat,L}$	1483	m/s
$p_{sat,L}$	4664.4	Pa
μ_L	10^{-3}	Pa.s

Vapour properties		
C	27234.7	Pa/(kg/m^3)$^\gamma$
γ	1.33	(-)
$\rho_{sat,V}$	0.0171	kg/m^3
$c_{sat,V}$	97.9	m/s
$p_{sat,V}$	125	Pa
μ_V	$9.75\cdot10^{-6}$	Pa.s

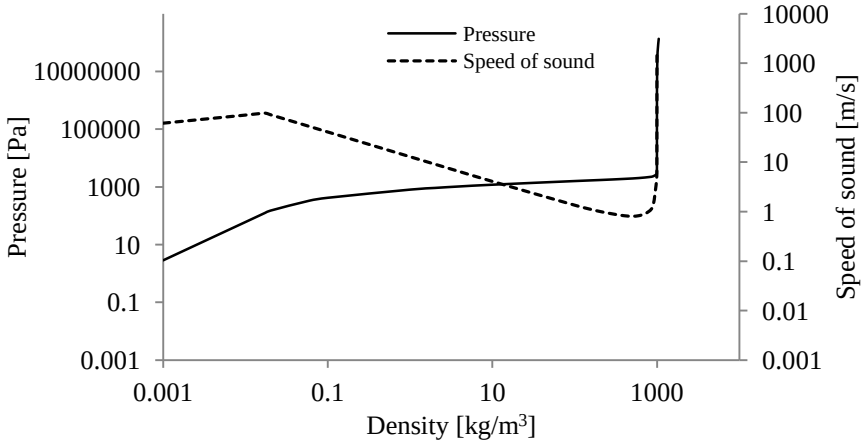

Figure 1. A graph showing the behaviour of the barotropic HEM EOS and the speed of sound variation.

2.3. Cavitation modelling: the two phase mixture model

The two phase mixture model, assumes mechanical equilibrium between the two phases, i.e. both liquid and vapour phase share the same pressure and velocity fields. An additional advection equation corresponding to the vapour fraction is solved, in the following form:

$$\frac{\partial(a\rho_v)}{\partial t} + \nabla(a\rho_v \mathbf{u}) = R_e - R_c \tag{7}$$

where a is the vapour fraction, ρ_v is the vapour density, **u** is the velocity field and R_e, R_c are the mass transfer rates for condensation (c) and evaporation (e). These terms are commonly associated with semi-empirical bubble dynamic models, based on the simplified, asymptotic Rayleigh-Plesset equation, but include additional user calibrated terms; two commonly used models, that will be examined in this study are the Zwart-Gerber-Belamri (ZGB) [26] and Schnerr-Sauer (SS) models [25]. In fact, the two phase model could be treated as a non-thermodynamic equilibrium model and an increase of the mass transfer rates R_e and R_c towards infinity will push the model towards thermodynamic equilibrium. Thus, for low mass transfer rates, it is not uncommon to observe regions of negative pressures. While negative pressures, or tension, has been found in delicate experiments in liquids (for

example [1, 34, 38]), one could question the existence of such cases in industrial scenarios. Especially for water in cavitation tunnels there is evidence that pressure at the cavitation region matches closely the saturation pressure at the given temperature [39]. So, in practice, one may have to tune the mass transfer terms in order to prevent as much as possible the existence of negative pressure zones.

For applying the two phase model, one needs to specify the properties and equation of state for the different materials. For the liquid phase either the incompressible assumption or the Tait equation of state is used. On the other hand, the gas/vapour phase is assumed to be incompressible. It must be highlighted here that even if the pure vapour phase is incompressible, the mixture is not, since mass transfer is involved; actually, the mass transfer is the dominant term affecting mixture compressibility [1]. The properties used for the materials involved are summarized in the following table; for the incompressible liquid, bulk modulus B and speed of sound c are no longer applicable.

Table II. Thermodynamic properties for water/vapour with the 2-phase model, values have been selected an saturation properties of water/steam at 20°C [37].

Liquid properties		
B	$307.1 \cdot 10^6$	Pa
n	7.15	(-)
$\rho_{sat,L}$	998.16	kg/m^3
$c_{sat,L}$	1483	m/s
$p_{sat,L}$	2340	Pa
μ_L	10^{-3}	Pa.s

Vapour properties		
$\rho_{sat,V}$	0.0171	kg/m^3
μ_V	$9.75 \cdot 10^{-6}$	Pa.s

3. Square Throttle Case and Simulation Setup

The experimental setup is extensively reported in the reference study [23], so the operating conditions and geometry are only briefly presented here. Water is discharged into a rectangular step nozzle with 48 ml/s flow rate and the outlet is subjected to atmospheric pressure. At these conditions a

recirculation region forms downstream the sharp step constriction and cavitation develops at the shear layer between the recirculation zone and the formed jet [23].

The dimensions of the constriction are 1.94x1.94x8mm (W×H×L) and the schematic of the nozzle is shown in Figure 2a along with velocity measurement positions. It should be noted that in the simulations the outlet is not placed directly at the end of the throttle, but rather further downstream in order to minimise its interference to the flow pattern developing in the throttle (see Figure 2b). The average velocity through the nozzle is 12.8m/s and the Reynolds number is Re=27000; these conditions correspond to incipient cavitation with cavitation number:

$$\sigma = \frac{p_{amb} - p_{vap}}{\frac{1}{2}\rho u^2} = 1.2 \tag{8}$$

where p_{amb} is the ambient pressure (atmospheric), p_{vap} is the vapour pressure, ρ the liquid density and u the characteristic velocity. Also, for the sake of completeness, we provide the value of an alternative definition for the cavitation number, denoted as CN, equal to $1/\sigma$; for the specific case CN=0.83. Based on these characteristics it is possible to make an estimate of the Kolmogorov scales and Taylor microscale of fluid motion for this case [29]:

$$\text{Kolmogorov length scale } \eta = \left(\frac{v^3}{\varepsilon}\right)^{1/4} = 0.98\mu\text{m} \tag{9}$$

$$\text{Kolmogorov time scale } \tau_\eta = \left(\frac{v}{\varepsilon}\right)^{1/2} = 0.96\mu\text{s} \tag{10}$$

$$\text{Taylor length scale } \lambda_g = \sqrt{10}\,\text{Re}^{-0.5}\,L = 39\mu\text{m} \tag{11}$$

where v is the kinematic viscosity which is ~10^{-6}m^2/s for water, ε is the turbulent dissipation, estimated roughly as u^3/L, with u a characteristic velocity, e.g. 12.8m/s, and L a characteristic length scale, e.g. 1.94mm. For the LES studies, as an initial guideline for the mesh sizing we have used a common

practice in the relevant literature, suggesting a grid size of the order of the Taylor length scale, since it lies at the dissipation region end of the inertial subrange; this mainly applies for isotropic turbulence, so it is used as a rough estimate for the mesh generation. It must be stressed that apart from this practical guideline, the turbulent kinetic energy spectrum was examined, in order to make sure that it obeys the -5/3 law for the energy cascade, see Pope[29]. The interested reader is addressed to several references[40-42] discussing on the subject of grid sizing in LES for practical flows.

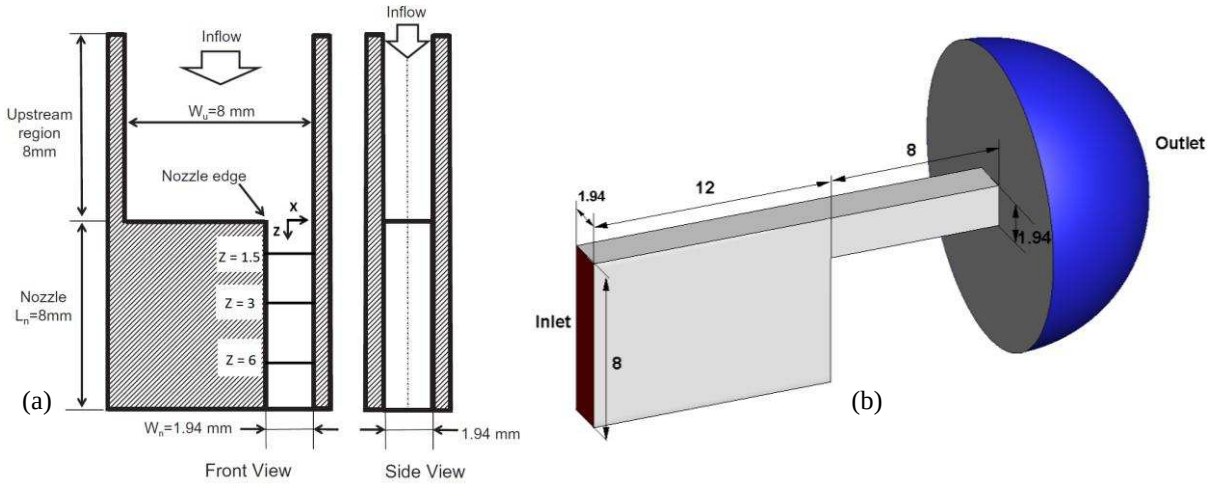

Figure 2. (a) Nozzle geometry [23] and (b) the computational domain used, with the boundary conditions shown; red corresponds to inlet, grey to walls and blue to outlet. All dimensions are in mm.

The simulations to be presented are detailed as follows:

1. First of all a grid dependence study was conducted with meshes of three different resolutions. These cases have been examined as single phase, for simplicity, and in steady state and imposed flow rate of 48ml/s. From these, the optimum resolution was determined for further examination with the rest RANS cases. Additionally, the total pressure at the inlet of the throttle for the given flow rate was determined and used as a convergence criterion for the grid dependence study and as a boundary condition for the rest of the simulations.

2. Then, the influence of the RANS models is examined. The models investigated are the Realizable k-ε, k-ω SST and the RSM. Again, these cases are examined under steady state.

3. The modified RNG k-ε and k-ω SST models have been further examined, with the Reboud et al. correction [15]. Since the improvement of this correction is related to the prediction of cavity shedding process, these cases are treated as unsteady.

4. The WALE LES model [24] is examined with various cavitation models, such as the Zwart-Gerber-Belamri, Schnerr-Sauer, Barotropic HEM and tuned Zwart-Gerber-Belamri. Due to the nature of the LES model, these cases are treated as unsteady too.

In all simulations at steps 2, 3 and 4, total pressure is imposed at the inlet, which is determined from step 1, and static pressure at the outlet. This combination works better for the transient cases, where partial blockage might be induced due to cavitation shedding and this might cause unrealistic pressure build-up at the inlet, should a fixed flow rate be imposed.

The computational mesh employed in all cases is block-structured. Mesh refinement with inflation layers, is employed in critical areas, such as in the vicinity of the walls. The average mesh resolution for the grid dependence study is 90μm, 75μm and 50μm, corresponding to 1M, 2.4M and 6.8M cells. The temporal resolution for the unsteady RANS is 1μs. For the LES mesh a similar mesh was used, with telescopic refinement to achieve high resolution in the area of interest (see Figure 3). The LES cell count is ~4M cells, but the spatial resolution is 20μm in the core of the throttle, while there is refinement towards the walls; the spatial resolution chosen is less than the Taylor length scale, based on practical guidelines. Given that an average velocity of ~12m/s occurs inside the throttle, a relevant time scale is 2μs. The time step size chosen is 1μs, which corresponds to a CFL number of 0.5, enough to properly describe the time scales of fluid motion. Based on the LES simulation results, y+ varies around 0.2-1 in the throttle. The near wall resolution is ~2.5μm, resulting to 6-7 cells within the viscous sublayer, which has a thickness of $\delta_s = 5 \cdot \nu/u_*$ ~15μm [29].

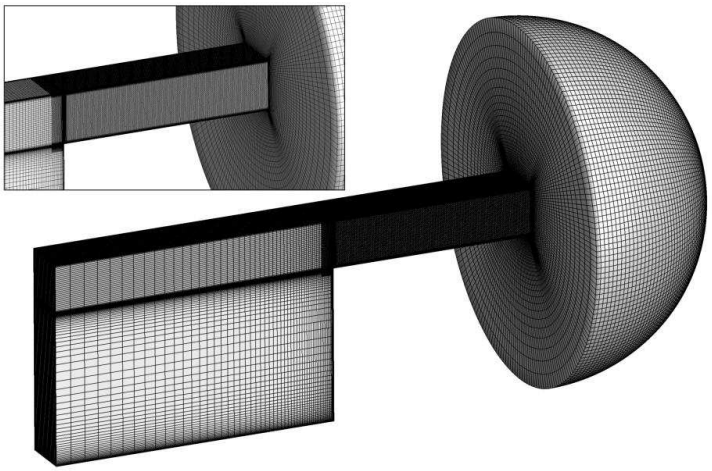

Figure 3. The LES mesh. The block-structured topology of the mesh is visible, as well as the telescopic refinement near the throttle entrance.

In all cases, the interest is on the average velocity distribution and RMS of velocity fluctuations in locations for which experimental measurements exist [23], i.e. at 1.5, 3 and 6mm downstream the edge of the throttle. It should be noted that since experimental data have been collected on the midplane of the geometry using Laser Doppler Velocimetry, this limits the information of the average velocity and RMS velocity fluctuations only to the x and z velocity components, see also the Front view, Figure 2.

Averaged fields are provided by steady state RANS by default, whereas RMS of velocity fluctuations are determined through total turbulent kinetic energy under the Boussinesq relationship for 2-eq. models [28], or directly from the computed Reynolds stresses, when the RSM model is used. For transient runs, such as LES, the time history of all velocity components is recorded and then the relevant components are used for comparisons. Qualitative comparisons of the cavitation pattern inside the throttle is examined when applicable.

4. Numerical results and comparison with experiments

4.1. Grid dependency test

As mentioned in the previous section, three different grid spacings have been tested to assess the sensitivity of the results on the mesh resolution. In this section the results will be presented for the k-ω

SST model; similar results have been obtained for other turbulence models. Grid dependency test results are reported in table III along with effect of grids on the total pressure at inlet. The calculated total pressure at inlet is affected less than 0.5%, giving confidence to use it as a boundary condition for the rest of the simulations. Moreover, all resolutions give a velocity distribution very similar to the experimental profile and the difference between subsequent refinements is not significant.

Table III. Grid parameters and their effect on total pressure at inlet.

Grid	Cells	Max y^+	Min y^+	Total pressure at inlet [Pa]
Coarse	1M	55	1	237260
Medium	2.3M	45	0.5	238270
Fine	6.8M	37	0.2	238220

Given the aforementioned results, the medium resolution is selected for the rest RANS studies, since it succeeds in capturing a velocity distribution very close to the experiment, while it does not predict a significantly different total pressure from the finest resolution employed.

4.2. Standard RANS models results

In this section the results from steady state RANS simulations will be discussed. All RANS models give an adequate prediction of the velocity distribution compared to experimental measurements of velocity inside the nozzle[23]. However, all the examined models fail to predict accurately the turbulent fluctuations near the nozzle exit at z = 6mm (see figure 2(a)). These discrepancies can be attributed to the steady state assumption of the flow and failure of all standard RANS models to predict cavitation.

Indeed, a very important observation, and an important conclusion of the present study, is that the steady state RANS models examined so far, fail to predict the onset of cavitation. To be more precise, the minimum pressure in the whole computational domain predicted by the models, as described so far, is:

- for the Realizable k-ε, 12970Pa

- for the k-ω SST, 10590Pa

- for the RSM, 13770Pa

It becomes clear that these minimum pressures are almost 5-6 times the saturation pressure of water, so cavitation is not predicted; in fact even applying corrections that increase the cavitation threshold pressure due to the influence of turbulence fluctuations (see e.g. [20]) still fail to produce cavitation. Assuming a cavitation threshold of the form:

$$p_v = p_{sat} + \frac{1}{2}(0.39k\rho) \tag{12}$$

where p_{sat} the saturation pressure, k the local turbulent kinetic energy and ρ the liquid density, the maximum threshold pressure for cavitation formation throughout the whole computational domain is:

- for the Realizable k-ε, 6515Pa

- for the k-ω SST, 7128Pa

- for the RSM, 8047Pa

which is still significantly lower, almost half, of the minimum liquid pressure that has been predicted in the computational domain by each model.

4.3. Modified URANS models results

Since it is suspected that part of the discrepancies is due to the steady state assumption of the flow, further examination of the case with unsteady RANS models has been conducted. Additionally, since it is known from the experiment that cavitation shedding occurs, due to the shear layer instabilities at the border of the recirculation zone, it was chosen to resort to the RANS modifications described in section 2.3, which are known to be able to predict such effects.

As shown in Figure 4, comparison between the modified URANS models and experimental data shows a close match in streamwise velocity profiles. It is notable that the velocity distribution matches closely to the experimental data at all locations z = 1.5, 3 and 6mm. The same observation applies for

366 the RMS of turbulent velocity fluctuation as well; note that the turbulent distribution has the correct
367 pattern at the location of z = 6mm, even though it is slightly underestimated.

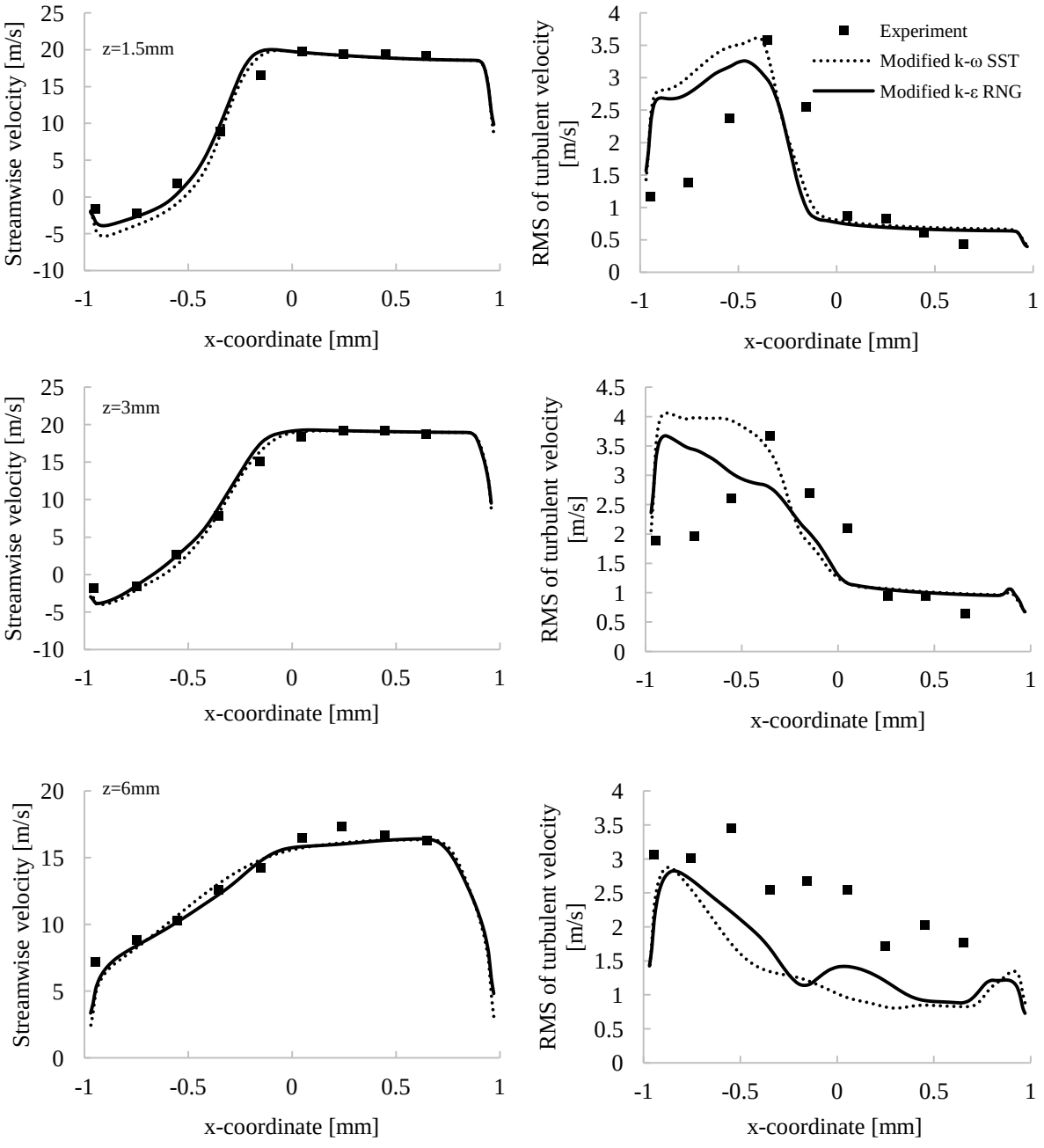

368
369
370

371 Figure 4. Streamwise velocity distribution and RMS of turbulent velocity at different locations downstream the
372 throttle edge, for different modified URANS models. The experimental results are indicated with squares.

373

A very important observation here is that still the unsteady RANS simulations failed to predict cavitation formation, even though flow unsteadiness has been observed. Since the nature of the correction is the reduction of turbulent viscosity in the mixture region, while reverting to the standard URANS formalism in the pure liquid/vapour phases, it is reasonable to conclude that the correction was not applied at all. To force the correction to operate, an amount of vapour was artificially introduced inside the recirculation region, in the centre of the large scale vortex, where pressure was lower, hoping that this would trigger cavity shedding. Unfortunately, even if unsteadiness temporarily was enhanced, after several time steps cavitation structures eventually collapsed, returning to the prior condition of pure liquid.

4.4. LES WALE results

The last results to be presented refer to the WALE LES model. In Figure 6 average velocity and RMS velocity fluctuations are shown, as before.

It is of interest that LES succeeds in predicting accurately the velocity distribution at all locations and provides very good estimates of the turbulent fluctuations both at the recirculation zone and the jet formed at the core of the throttle. Moreover cavitation is predicted with all cavitation models, predicting a very similar velocity profile, showing that the velocity distribution is rather weakly related to cavitation presence; this is explained by the low cavitation intensity of the examined configuration. The same applies for the average volume fraction distribution, as shown in Figure 5, for the examined models. Statistics were collected for 3000 time steps (or 3ms), thus slight scattering is present. However, the average cavitation development is similar for all cavitation models.

Considering the minimum pressures that develop inside the computational domain:

- The modified coefficient ZGB model, instantaneous minimum ~ -3000Pa and minimum average ~7200Pa.
- The barotropic model, instantaneous minimum ~500Pa and minimum average ~9800Pa.
- The standard ZGB model, instantaneous minimum ~ -12000Pa and minimum average ~7800Pa.
- The standard SS model, instantaneous minimum ~ -20000Pa and minimum average ~8600Pa.

The barotropic model is the only one that predicts a positive minimum pressure, due to the Homogenous Equilibrium assumption; in fact a negative pressure in the barotropic model does not have any meaning, since it corresponds to negative density and non-real speed of sound, see eq. 6. The other models, predict negative pressures which drive the mass transfer from liquid to vapour phases. Indicative flow instances are presented in Figure 7, showing the shedding of cavitation structures, the highly transient velocity and pressure distributions for the barotropic HEM.

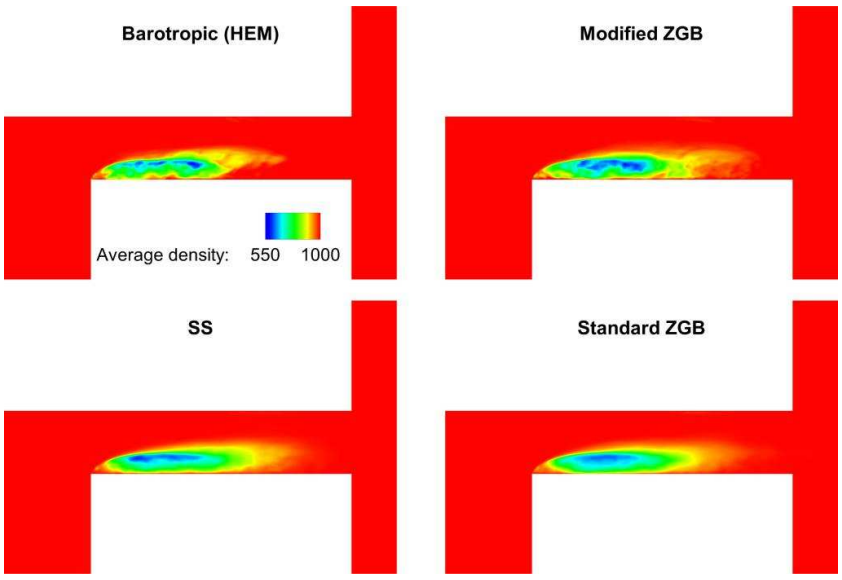

Figure 5. Indicative average density distribution downstream the constriction with several cavitation models, the barotropic HEM and the 2-phase modified ZGB, Schnerr Sauer and standard ZGB models. Units are in SI, i.e. [kg/m^3] for density.

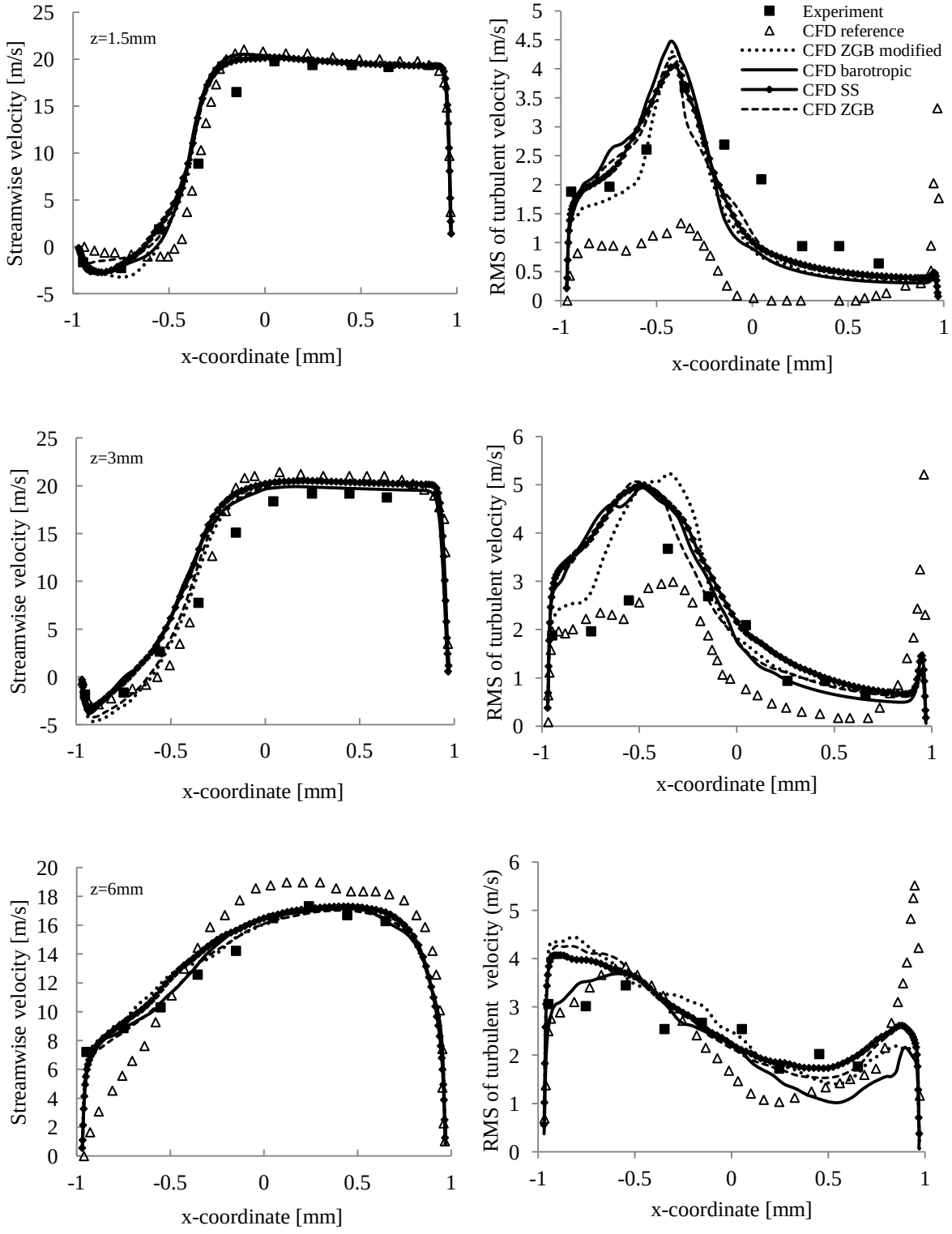

Figure 6. Average streamwise velocity distribution and RMS of turbulent velocity at different locations downstream the throttle edge, for LES and with different cavitation models. The experimental results are indicated with squares and the reference CFD results [23] with triangles.

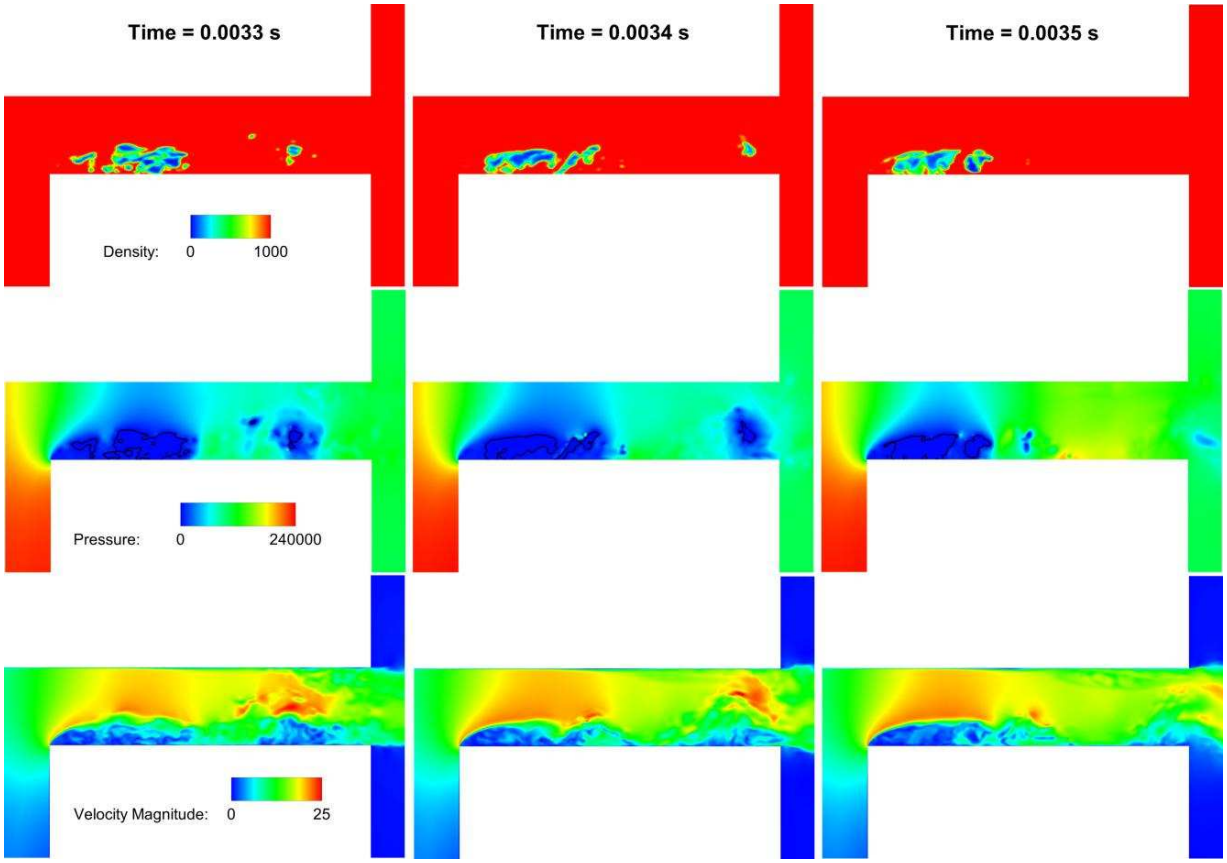

Figure 7. Barotropic HEM model: Instances of the instantaneous density, pressure field (the black line shows regions of pressure below saturation pressure) and velocity distribution at 0.1ms intervals. The high flow unsteadiness is clearly visible. Units are in SI, i.e. [kg/m^3] for density, [Pa] for pressure and [m/s] for velocity.

It is important to remark that even the LES model employed predicts an average pressure that is higher than the saturation pressure, in a similar fashion as the RANS simulations. However, instantaneously pressure inside the vortices formed due to the shear layer instabilities drops below saturation, causing the formation of highly transient cavitation structures.

5. Simulations in Diesel injector

In this section, results from the LES simulation of the flow inside a Cat® Diesel injector will be presented. It has to be kept in mind that a complete Diesel injector is a rather complicated device, involving the interaction of hydraulic, electrical and mechanical components, for more information the

interested reader is addressed to the work of Egler et al.[43]. The main focus here will be at the tip of the Diesel injector, as shown in Figure 8, where the main components, like needle, body and orifices, are shown. The injector is a 5-hole, tapered (k-factor equal to 1.1) common rail injector. The injector is operating at an inlet pressure level of ~1800bar and the outlet pressure is ~50bar. The exact discharge pressure and needle lift are provided in Figure 8, estimated through simplified 1-D analysis [44].

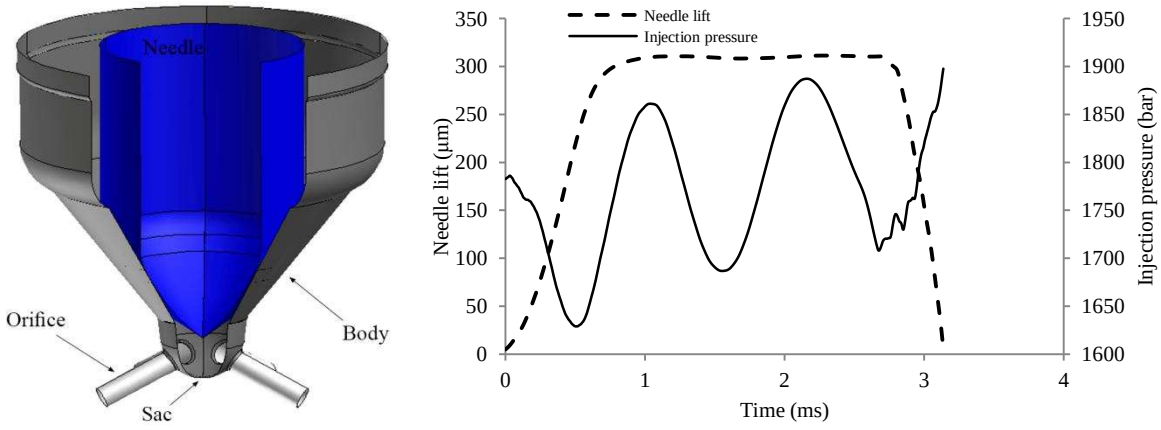

Figure 8. A simple sketch of the examined injector and the operating conditions (needle lift and inlet pressure).

The cavitation number for the injector is significantly lower than the simplified throttle presented in section 3, due to the immense pressure difference:

$$\sigma = \frac{p_{down} - p_{vap}}{p_{up} - p_{down}} = 0.028 \quad (13)$$

where p_{down} is the ambient/downstream pressure (50bar), p_{vap} is the vapor pressure (~1bar, based on Diesel properties at 400K, see also[44, 45]) and p_{up} is the upstream pressure of the injector (~1800bar). The CN value of the injector case is ~36. The properties used for the simulation are based on interpolation formulas from N. Kolev[45], derived at an average temperature of 400K, based on preliminary 1D analysis including heating effects[46]. Diesel density at saturation is $\rho_{L,sat}$ = 747.65kg/m^3,

Diesel vapor pressure is ~1.1bar, Diesel bulk modulus is ~110MPa and Diesel liquid viscosity is given by the following equation:

$$\log_{10}\left(10^6 \mu_L / \rho\right) = 0.035065275 - 0.000234373\,\mathrm{p}/10^5 \quad (14)$$

Diesel vapor density is 6.5kg/m^3 based on the ideal gas equation at the saturation pressure and temperature of 400K. Vapor viscosity is assumed constant and equal to 7.5μPa.s. Based on the aforementioned properties and velocity/spatial scales the Reynolds number is estimated to be ~30000 inside the orifice hole at high lift operation.

The computational meshes used for the injector analysis are hexa-dominant block meshes with structured and unstructured parts, with sufficient resolution depending on the assumptions of the models used; the RANS mesh had ~300000-500000 cells for low-lift and high-lift operation, whereas the LES mesh had a significantly higher resolution, starting at 10^6 cells at low lifts and peaking at $1.75 \cdot 10^6$ cells at high lifts. The LES resolution was based on the same guideline as in section 3, on the Taylor scale. Based on the orifice diameter, the Taylor length scale is λ_g~7μm, thus the grid sizing selected was of equal size and additional refinement was employed near the walls. Also, high resolution was maintained in critical areas of the injector, such as the needle/needle seat passage, which is represented with at least 6cells for RANS and 10cells for LES at the minimum lift of 5μm simulated. This number of cells is kept until a needle lift of ~40μm; beyond this point additional cell layers are added (during opening) or removed (during closing) to the needle seat/needle passage. Both cases solved only 1/5th of the whole injector tip, assuming only axial needle motion and symmetry boundary conditions for RANS, or periodic boundary conditions for LES, at the sides of the computational slice solved.

Several simulations have been performed with RANS models, including the RNG k-espilon model with Reboud correction, described in eq. 1 and the WALE LES model. The simulations to be presented hereafter omit heating effects, mainly due to increased complexity and problematic behavior

of the polynomial relations at high pressures and temperatures. In RANS simulations the effect of constant density and viscosity (set as the average based on the inlet and outlet conditions) as well as varying density and viscosity was examined. For the LES case the modified ZGB model was used, along with the Tait equation of state for the liquid. It is reminded that the modified ZGB model has increased mass transfer rates for condensation and evaporation, in order to move the phase change process closer to thermodynamic equilibrium. Standard cavitation models are prone to predicting unrealistically high tension in the liquid, of the order of -300bar for Diesel injection cases, see also the relevant work from Koukouvinis et al.[44, 47]. Increasing the mass transfer greatly reduces this tension, at least by an order of magnitude, moving much closer to the saturation pressure. Moreover, high mass transfer rates lead to replication of the Rayleigh collapse of vapor structures (for more information see the Appendix B section), which is essential if one desires to capture pressure peaks from the cavity collapses that could be linked to erosion. Unfortunately, the very time consuming nature of LES simulations did not permit testing of different models, e.g. testing the barotropic model or constant fuel properties. However the LES set-up discussed here has been found to predict a very similar pressure peak pattern in comparison to relevant experiments, see [44], which we consider, acts as a validation.

The flow field results of the RANS simulations were very similar, irrespectively of using varying or constant density/viscosity. While there is a notable increase in the mass flow rate of ~5%, when varying density/viscosity is used, the macroscopic appearance of the flow field is the same. For example, in Figure 9 the vapour fraction distribution inside the orifice hole is shown for the varying density for several instances of the high lift operation, simulated with the RNG k-epsilon model with Reboud correction. Despite some unsteadiness at the opening and closing phases on the injection, during the high lift operation there is practically a steady attached cavity at the upper surface of the orifice hole that maintains its size, topology and shape throughout the whole high lift operation. This seems contradictory to real injector visualization studies, where cavity shedding and cavitating

vortices are found, see for example the work of Mitroglou et al.[48]. Contrary to RANS, LES predicts a much more unsteady vapor field, with an attached cavity at the upper hole surface that grows and shrinks over time, periodic cavity shedding and occasional formation of cavitating vortices. Here it should be mentioned that in cases of injectors with cylindrical holes (no tapering), unsteady flow was predicted with the modified RANS model described above, as well as the LES model.

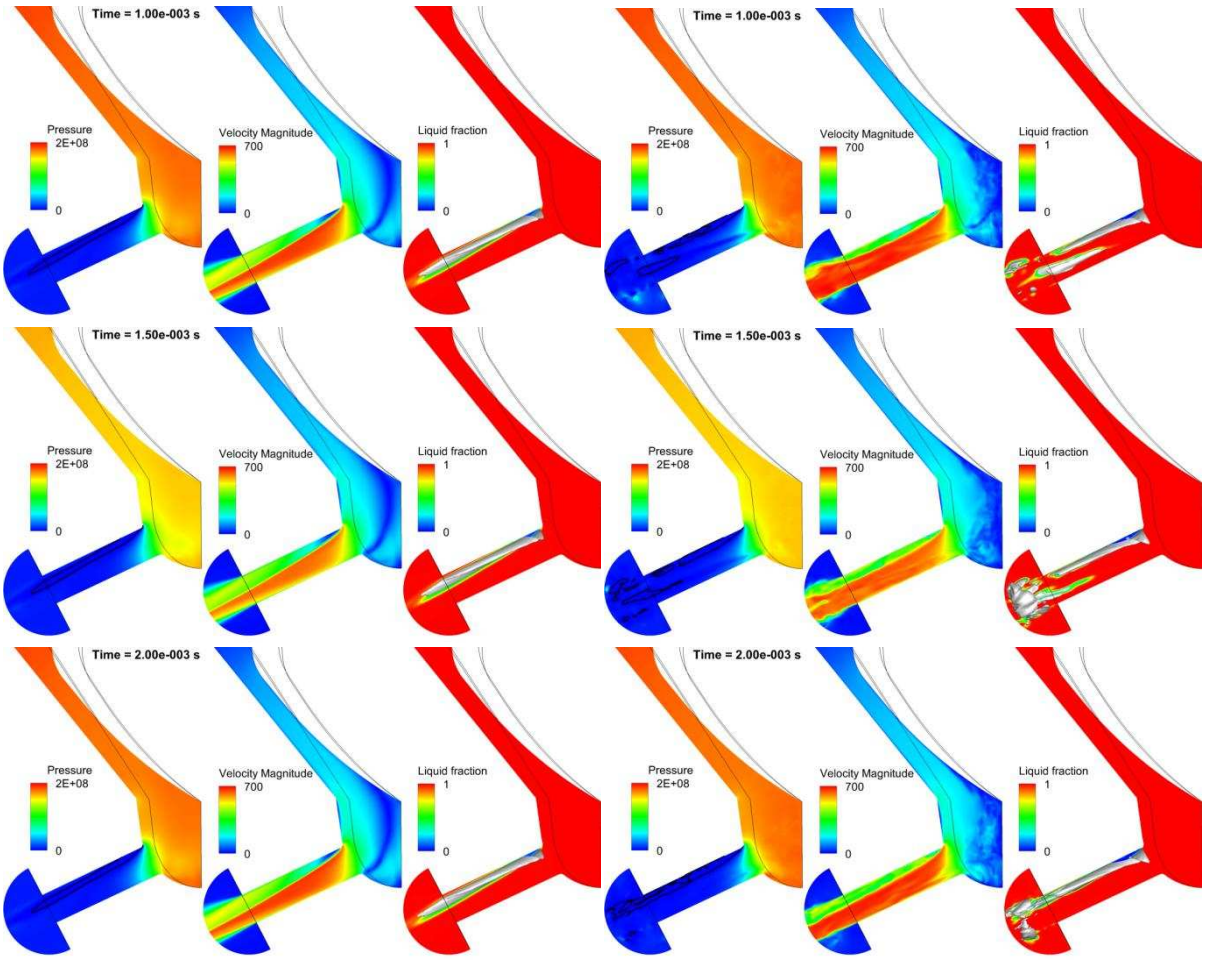

Figure 9. RANS (left) and LES (right) flow field at the midplane of the injector, for several instances at high lift operation. Pressure (Pa), Velocity magnitude (m/s) and liquid volume fraction are shown at the slice; the thick black line in the pressure slice denotes the region where pressure is lower the saturation and the grey isosurface represents the surface at 0.5 vapour volume fraction. Note the significant instability of the flow field with occasional appearance of cavitating vortices, as predicted with LES.

6. Discussion

From the results presented so far there are several important conclusions reached. First of all, it is found that traditional RANS turbulence models may fail to predict a correct flow field in conjunction with cavitation, both at low and high cavitation numbers. Indeed, the tight coupling of cavitation with vortices, requires the accurate prediction of vortical structures in the flow, since those may contribute to the generation and transport of cavitation formations. RANS models are not very well suited in this role, since by their principle of operation, they do not aim to predict vortices, but rather a mean flow path, compensating for unresolved structures with the addition of turbulent viscosity. While some corrections to take into account turbulent fluctuations [19, 20] and modifications to predict shedding exist [13-15, 32], their applicability seems case dependent and situational. These conclusions are supported by other studies in literature as well [21]. Contrary to RANS/URANS models, Large Eddy Simulation proven able to predict correctly both the averaged velocity profiles and the cavitation formation mechanism at incipient cavitation (high σ, low CN), since it inherently aims to capture the larger eddies that can contribute to cavitation development. Considering the injector results, at high intensity cavitation (low σ, high CN), while modified RANS is capable of predicting cavitation, an unphysically stable cavity is found, that contradicts experimental evidence. On the other hand, the examined LES model predicts a proper cavity shedding and relevant instabilities; while in the injector case no validation on the velocity field is available, recording of the pressure peaks due to vapor structure collapse correlates well with the erosion pattern found in experiments, indicating a reasonable reproduction of the vaporous flow structures.

In any case, from the results so far it seems that transient simulation is more successful in capturing the velocity distribution, even for RANS. Of course it is easy to understand that unsteady simulations, and even more LES with its special grid requirements, are rather intensive to resolve. However, given the observed deficiency of standard RANS models to predict the correct flow in many cases, it seems

that LES/DES or similar scale resolving methods are essential for the proper flow representation. Alternatively, it could be the case that there is a need for the development of new turbulence models that can correlate turbulent characteristics with cavitation in a better way than existing models. In any case, one should not forget that many turbulence models have been developed in the past, but still each of them has limited applicability. In other words such an effort might lead to another situational RANS model that performs well in some cases and bad in others; after all, the need to resort in scale resolving simulations more and more, even in industrial level, could mean that the level of accuracy required nowadays justifies the use of more computationally expensive models such as LES. Undeniably, RANS models can (and will) still play a role in industrial numerical simulations, since they can offer a solution very fast, being ideal for e.g. design/optimization studies.

Regarding the influence of the cavitation model, it seems that at low intensity cavitation it did not play a significant role in the average flow pattern. While to reach a final conclusion a quantitative comparison of vapor fraction distribution is required, relevant data are not available and in general are difficult to obtain. This forces to resort to qualitative comparisons of indicative cavitation instances, which clearly show a cavitation shedding mechanism. Also, from the aforementioned results, it is visible that the increased mass transfer rates of the modified ZGB model result to moving closer to thermodynamic equilibrium and reduction of the magnitude of negative pressures. Whereas in the enlarged nozzle case this does not seem to have a pronounced effect to the macroscopic characteristics of the flow field, this is not the case at high intensity cavitation cases, like the flow inside the real injector. As discussed in the relevant section, the standard formulation of commonly used cavitation models lead to unrealistically high liquid tension. Thus in such cases it is essential to modify the cavitation model accordingly, in order to move closer to thermodynamic equilibrium. Unfortunately how close to or far from thermodynamic equilibrium each case is, is not known a priori. For water there is some evidence that cavitation behaves as a thermodynamic equilibrium process, see the interesting work of Washio[39]. It is our opinion that more fundamental work is required on the

thermodynamics of fluids, for the understanding of meta-stability that affects cavitation and other effects such as flashing.

7. Conclusion

This paper evaluates the predictive capability of 2-equation and 7-equation RANS models to simulate incipient cavitation in an enlarged rectangular step nozzle and developed cavitation in an actual Diesel injector, and compares the results with WALE LES model predictions. The LES model is also used to further investigate the performance of barotropic and 2-phase mass transfer cavitation models.

Both cases show the situational applicability of RANS model for predicting cavitation. For the enlarged step nozzle, all the RANS models used, i.e. the Realizable k-ε, SST k-ω and RSM model failed to predict pressures below the saturation pressure. RANS is a useful tool for many cavitation problems as seen in the literature, but its limited capability has also been reported for cases with small amounts of cavitation [21]. For problems such as incipient cavitation in a nozzle where the pressure drop from inlet to outlet is low, small vortices are formed that act as nucleation sites for bubbles. In order to capture these flow structures, more rigorous turbulence models such as LES are required. The average minimum pressure predicted by the barotropic and the non-equilibrium cavitation models is above the saturation pressure of water. This result further justifies the minimum pressure predicted by RANS models, which is above saturation pressure. Furthermore, changing the cavitation model did not significantly affect the streamwise velocity outside the cavitation region. The predicted shape of the cavity was in agreement with experimental images, however quantitative measurements inside the vapour volume is required to judge the accuracy of the calculated cavitation.

At high cavitation intensity RANS models may predict cavitation, but the predicted structure may be unrealistically stable, especially in cases of hole tapering where orifice turbulence is suppressed. The LES model tested was found able to reproduce an unsteady flow field, even in the cases of tapered

holes, but comes with a very high price, since the associated computational cost is significantly higher than that of RANS. Just for reference, an LES simulation may require 20x the time of an URANS simulation and maybe more than 1000x the time needed for a steady state RANS simulation. Potentially, the future lies on scale adaptive models and RANS/LES hybrids, such as Detached Eddy Simulation.

Acknowledgements

The research leading to these results has received funding from the People Programme (IAPP Marie Curie Actions) of the European Union's Seventh Framework Programme FP7/2007-2013/ under REA grant agreement n. 324313. We have also to thank Caterpillar Inc. for providing the injector geometries, operating conditions and experimental results regarding erosion.

Disclaimer

Nomenclature

a	Vapor fraction (-)
ρ	Density (kg/m^3)
μ_t	Turbulent viscosity (Pa.s)
v	Kinematic viscosity (m^2/s)
k	Turbulent kinetic energy (m^2/s^2)
ε	Turbulent dissipation (m^2/s^3)

ω	Specific dissipation rate (1/s)
S_{ij}	Strain rate tensor, ij component (1/s)
c	Speed of sound (m/s)
p	Pressure (Pa)
B	Bulk modulus (Pa)
u	Velocity vector field (m/s)
R_e, R_c	Evaporation and condensation source terms for the 2-phase model (kg/s/m^3)
σ	Cavitation number (-)
CN	Alternative definition of cavitation number, equal to $1/\sigma$ (-)
η	Kolmogorov length scale (m)
τ_η	Kolmogorov temporal scale (m)
λ_g	Taylor length scale (m)
u*	Friction velocity (m/s)
δ_s	Viscous sublayer thickness (m)

Appendix A: Derivation of the mixture part equation of state.

Starting with the definition of the speed of sound:

$$c^2 = \left(\frac{\partial p}{\partial \rho}\right)_S \tag{15}$$

and the Wallis speed of sound for bubbly mixtures:

$$\frac{1}{c_m^{\,2}\rho_m} = \frac{a_l}{c_l^{\,2}\rho_l} + \frac{a_v}{c_v^{\,2}\rho_v} \tag{16}$$

one may formulate pressure as:

$$p = \int c^2 d\rho + p_{ref} \Rightarrow$$

$$p = \int \left[\rho\left(\frac{1-a_v}{c_l^{\,2}\rho_l} + \frac{a_v}{c_v^{\,2}\rho_v}\right)\right]^{-1} d\rho + p_{ref} \tag{17}$$

where the vapour fraction is a function of density:

$$a_v = \frac{\rho - \rho_v}{\rho_l - \rho_v} \tag{18}$$

The result of the integration in eq. 17, considering also eq. 18 is shown below:

$$p = \frac{c_v c_l (\rho_v - \rho_l)\rho_v \rho_l}{\rho_v^2 c_v^2 - \rho_l^2 c_l^2}\left[\ln(\rho) - \ln\left[c_v^2 \rho_v (\rho - \rho_v) + c_l^2 \rho_l (\rho_l - \rho)\right]\right] + p_{ref} \tag{19}$$

Based on logarithm properties, eq. 19 may be written as:

$$p = \frac{c_v c_l (\rho_v - \rho_l)\rho_v \rho_l}{\rho_v^2 c_v^2 - \rho_l^2 c_l^2} \ln\left(\frac{\rho}{c_v^2 \rho_v (\rho - \rho_v) + c_l^2 \rho_l (\rho_l - \rho)}\right) + p_{ref} \tag{20}$$

which is the mixture relation in the HEM EOS (eq. 6), valid only when density is between liquid and vapour saturation densities, i.e. $\rho_l \geq \rho > \rho_v$.

Appendix B: Comparison between the 2-phase and barotropic models in fundamental cases.

In this section a comparison between the 2-phase mass transfer and barotropic models is discussed in a more fundamental basis, in order to show clearly the effect of their assumptions. Moreover, the influence of the mass transfer rate is examined.

A first case examined is a shock tube case. The shock tube is a fundamental test of compressible flows where a simple 1D flow is considered. There are two distinct states, the left state (L, for x<0m) and right state (R, for $x \geq 0$m), separated by an initial discontinuity at x=0m. The two states that are examined here are pure diesel liquid as the left state, at a pressure of 100bar, and a liquid/vapour mixture, at saturation pressure (~892Pa) and 90% vapour fraction. The thermodynamic model for the materials is either the 2-phase mixture or barotropic HEM, as discussed in sections 2.2 and 2.3. An exact solution of the problem for the barotropic HEM model may be derived using the Rankine-Hugoniot conditions and Riemann invariants, see the book of Toro[49]. As will be shown later, the exact solution can serve as an asymptotic solution for the 2-phase mass transfer model as well, when the

mass transfer is high enough. It has to be highlighted that the solution of the Riemann problem for such equations of state is not trivial; the interested reader is addressed to the recent work of Koukouvinis et al.[50] for more information about the exact solver. The numerical solution is obtained using 1000 cells in the x direction.

In Figure 10, a comparison between the numerical and exact solutions between the models is shown at time of 1ms. As it is visible, the exact solution and the barotropic HEM solution match perfectly, which also acts as a validation of the described methodology in section 2.3. The 2-phase solution is greatly dependent on the mass transfer rate, see the source term of eq. 7. For high mass transfer rates (which are represented by the dark red cycles in Figure 10), the solution converges to the exact barotropic HEM solution. This is reasonable, because the mass transfer term affects the mixture speed of sound; increasing the mass transfer results to a decreased mixture speed of sound, see also Franc[1]. On the other hand, when the mass transfer term is low, then the mixture speed of sound increases, leading a more diffused profile in the velocity distribution (see the light red, orange and yellow circles in Figure 10). The same effect is found in density field as well, but it is much less observable. Each 2-phase mixture solution has an increase in the mass transfer rate by one order of magnitude, i.e. the dark red cycles solution has a 10^4 higher mass transfer rate than the light yellow reference solution.

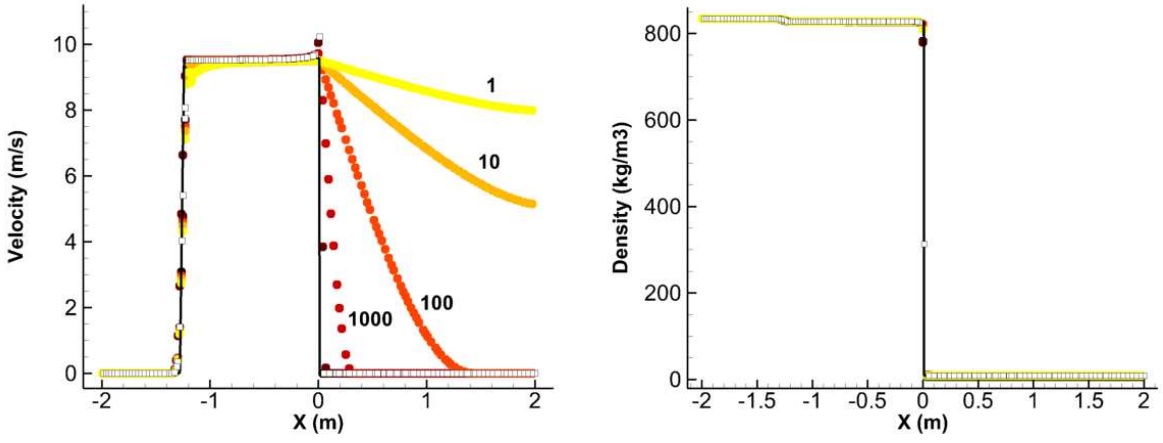

Figure 10. Shock tube case, comparison between various models at t = 1ms. Continuous line is the exact solution, white filled squares are the numerical barotropic HEM solution and coloured cycles are the 2-phase mass transfer solution. The colour of the cycles represents the magnitude of the mass transfer term, which is mentioned in text also near the respective line: yellow (1x multiplier for the reference mass transfer) for low mass transfer rates to dark red (10^4x multiplier for the reference mass transfer) for high mass transfer rates.

Another test case, commonly used in cavitating flows, is the Rayleigh collapse. A sphere of vapour is subjected to compression due to the influence of the surrounding high pressure liquid. This case has an exact and well known solution, where the radius of the bubble reduces in an accelerating manner, with bubble wall velocity tending to infinity, see e.g. Franc[1]. In that case, the bubble collapse velocity, dR/dt, is given by the following relation:

$$\frac{dR}{dt} = -\sqrt{\frac{2}{3}\frac{p_\infty - p_v}{\rho}\left[\left(\frac{R_0}{R}\right)^3 - 1\right]} \tag{21}$$

where:

- p_∞ is the pressure at the farfield
- p_v is the vapour pressure
- ρ is the liquid density
- R_0 is the initial bubble radius and R is the current bubble radius

By integrating the bubble wall motion, it is possible to find the bubble collapse time:

$$\tau \cong 0.915 R_0 \sqrt{\frac{\rho}{p_\infty - p_v}} \tag{22}$$

Here, the collapse of water vapour bubble at pressure p_v = 2339Pa and initial radius R_0=10μm is examined. The case is resolved as 2D axis-symmetric simulation, with a 60000 cells. Indicative results are shown in Figure 11, where the theoretical evolution of the bubble radius is compared with the numerical solutions. In order to have a fair comparison, both models were simulated with a timestep of 1ns. For the 2-phase model, it is clear that only at a high mass transfer rate the proper behaviour of the Rayleigh collapse is replicated. The barotropic HEM model predicts a bubble collapse very close to the theoretical. The mismatch is found to be due to the timestep; the higher the convective Courant number, the more diffuse the bubble interface becomes with the HEM model. Significantly reducing the timestep greatly improves the agreement with the theoretical solution.

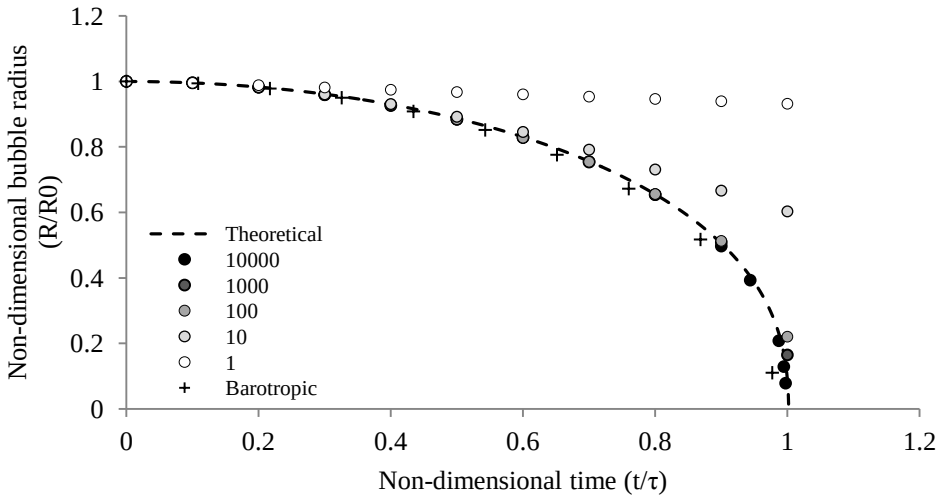

Figure 11. Rayleigh collapse test case, comparison of the bubble radius evolution for various models. The dashed line shows the exact solution, crosses the barotropic model HEM solution, whereas circles the 2-phase model solution (the mass transfer is higher for dark circles and lower for whiter circles, a reference multiplier is given in legend).

From the discussed examples, the conclusion is that the 2-phase mass transfer model and barotropic HEM model are equivalent for high mass transfer rates of the latter. Other practical comparisons of the two models, in e.g. throttle flows, may be found in a recent work of Koukouvinis et al.[47], supporting the aforementioned conclusion.

References

1. Franc J-P and Michel J-M. Fundamentals of Cavitation. Kluwer Academic Publishers, 2005.

2. Afzal H, Arcoumanis C, Gavaises M and Kampanis N. Internal flow in diesel injector nozzles: modelling and experiments. IMechE Paper S. 1999; 492: 25-44.

3. Andriotis A, Gavaises M and Arcoumanis C. Vortex flow and cavitation in diesel injector nozzles. Journal of Fluid Mechanics. 2008; 610: 195-215.

4. Arndt RE. Cavitation in vortical flows. Annual Review of Fluid Mechanics. 2002; 34: 143-75.

5. Pozrikidis C. Fluid dynamics: theory, computation, and numerical simulation. Springer Science & Business Media, 2009.

6. Laberteaux K and Ceccio S. Partial cavity flows. Part 1. Cavities forming on models without spanwise variation. Journal of Fluid Mechanics. 2001; 431: 1-41.

7. Bin J, Luo X-w, Peng X-x and Wu Y-l. Three-dimensional large eddy simulation and vorticity analysis of unsteady cavitating flow around a twisted hydrofoil. Journal of Hydrodynamics, Ser B. 2013; 25: 510-9.

8. Chahine G and Genoux PF. Collapse of a cavitating vortex ring. Journal of fluids engineering. 1983; 105: 400-5.

9. Simpson RL. Turbulent boundary-layer separation. Annual Review of Fluid Mechanics. 1989; 21: 205-32.

10. Iyer CO and Ceccio SL. The influence of developed cavitation on the flow of a turbulent shear layer Physics of Fluids 2002; 14: 3414-31.

11. Okabayashi K and Kajishima T. Investigation of turbulent modulation by cavitation for subgrid-scale modeling in LES CAV2009. Ann Arbor, Michigan, USA2009.

12. Dular M and Delgosha OC. Numerical modelling of cavitation erosion. International Journal for Numerical Methods in Fluids. 2009; 61: 1388–410.

13. O. Coutier-Delgosha, J. L. Reboud and Delannoy Y. Numerical simulation of the unsteady behaviour of cavitating flows. International Journal for Numerical Methods in Fluids. 2003; 42: 527-48.

14. O. Coutier-Delgosha, J. L. Reboud and Fortes-Patella R. Evaluation of the Turbulence Model Influence on the Numerical Simulations of Unsteady Cavitation. Journal of Fluids Engineering. 2003; 125: 38-45.

15. Reboud J-L, Stutz B and Coutier O. Two-phase flow structure of cavitation: experiment and modelling of unsteady effects. Third International Symposium on Cavitation. Grenoble, France1998.

16. Decaix J and Goncalvès E. Compressible effects modeling in turbulent cavitating flows. European Journal of Mechanics - B/Fluids. 2013; 39: 11-31.

17. Wu J, Wang G and Shyy W. Time-dependent turbulent cavitating flow computations with interfacial transport and filter-based models. International Journal for Numerical Methods in Fluids. 2005; 49: 739-61.

18. Decaix J and Goncalvès E. Time-dependent simulation of cavitating flow with $k-\ell$ turbulence models. International Journal for Numerical Methods in Fluids. 2012; 68: 1053-72.

19. Giannadakis E. Modelling of Cavitation in Automotive Fuel Injector Nozzles. Department of Mechanical Engineering. University of London, 2005, p. 431.

20. Singhal AK, Athavale M, Li H and Jiang Y. Mathematical Basis and Validation of the Full Cavitation Model Journal of Fluids Engineering. 2002; 124: 617-24.

21. Edelbauer W, Strucl J and Morozov A. Large Eddy Simulation of cavitating throttle flow. SimHydro 2014:Modelling of rapid transitory flows. Sophia Antipolis2014.

22. Örley F, Hickel S, Schmidt SJ and Adams NA. LES of cavitating flow inside a Diesel injector including dynamic needle movement. Journal of Physics: Conference Series. 2015; 656.

23. Sou A, Bicer B and Tomiyama A. Numerical simulation of incipient cavitation flow in a nozzle of fuel injector. Computers & Fluids 2014; 103: 42 - 48.

24. Ducros F, Nicoud F and Poinsot T. Subgrid-scale modeling based on the square of the velocity gradient tensor flow. Turbulence and Combustion. 1999; 62: 183-200.

25. Schnerr GH and Sauer J. Physical and numerical modelling of unsteady cavitation dynamics. Proceedings ICMF-2001 – 4th International Conference on Multiphase Flow. New Orleans, USA2001.

26. Zwart PJ, Gerber AG and Belamri T. A two-phase flow model for predicting cavitation dynamics 5th International Conference on Multiphase Flow Yokohama, Japan2004.

27. Schmidt D. Cavitation in Diesel Fuel Injector Nozzles. University of Wisconsin - Madison, 1997.

761 28. Versteeg H and Malalsekera W. An Introduction to Computational Fluid Dynamics: The
762 Finite Volume Method. Prentice Hall, 2007.
763 29. Pope S. Turbulent Flows. Cambridge University Press, 2000.
764 30. Wilcox D. Turbulence Modeling for CFD. D C W Industries, 2006.
765 31. Launder BE. Second-moment closure and its use in modelling turbulent industrial flows.
766 International Journal for Numerical Methods in Fluids. 1989; 9: 963-85.
767 32. Delgosha OC, Patella F and Reboud J-L. Simulation of unsteady cavitation with a two-
768 equation turbulence model including compressibility effects. Journal of Turbulence. 2002; 3.
769 33. Sarkar S and Lakshmanan B. Application of a Reynolds stress turbulence model to the
770 compressible shear layer. AIAA Journal. 1991; 29: 743-9.
771 34. Brennen C. Cavitation and Bubble Dynamics. Oxford University Press, 1995.
772 35. Koop AH. Numerical Simulation of Unsteady Three-Dimensional Sheet Cavitation.
773 University of Twente, 2008.
774 36. Ivings MJ, Causon DM and Toro EF. On Riemann solvers for compressible liquids.
775 International Numerical Methods for Fluids. 1998; 28: 395-418.
776 37. Holmgren M. X-steam v2.6, http://xsteam.sourceforge.net/.
777 38. Caupin F and Stroock AD. The Stability Limit and other Open Questions on Water at
778 Negative Pressure. Liquid Polymorphism. 2013; 152.
779 39. Washio S. Recent Developments in Cavitation Mechanisms: Cavitation inception in
780 separating water flows. A Guide for Scientists and Engineers. Elsevier, 2014, p. 133-57.
781 40. Addad Y, Gaitonde U, Laurence D and Rolfo S. Optimal Unstructured Meshing for Large
782 Eddy Simulations. In: Meyers J, Geurts B and Sagaut P, (eds.). Quality and Reliability of Large-Eddy
783 Simulations. Netherlands: Springer, 2008.
784 41. Bogey C and Bailly C. Influence of Reynolds number and grid resolution on large-eddy
785 simulations of self-similar jets based on relaxation filtering. In: Salvetti MV, Geurts B, Meyers J and
786 Sagaut P, (eds.). Quality and Reliability of Large-Eddy Simulations II. Netherlands: Springer, 2011.

42. Sagaut P. Large Eddy Simulation for Incompressible Flows: An Introduction. Berlin: Springer-Verlag 2006.

43. Egler W, Giersch JR, Boecking F, et al. Fuel Injection Systems. In: Mollenhauer K and Tschöke H, (eds.). Handbook of Diesel Engines. 1 ed.: Springer-Verlag Berlin Heidelberg, 2010, p. 127-74.

44. Koukouvinis P, Gavaises M, Li J and Wang L. Large Eddy Simulation of Diesel injector including cavitation effects and correlation to erosion damage. Fuel. 2016; 175: 26-39.

45. Kolev N. Multiphase Flow Dynamics 3. Springer Berlin Heidelberg, 2007.

46. Strotos G, Koukouvinis P, Theodorakakos A, Gavaises M and Bergeles G. Transient heating effects in high pressure Diesel injector nozzles. International Journal of Heat and Fluid Flow. 2015; 51: 257-67.

47. Koukouvinis P and Gavaises M. Simulation of throttle flow with two phase and single phase homogenous equilibrium model. Journal of Physics: Conference Series. 2015; 656: 012086.

48. Mitroglou N, McLorn M, Gavaises M, Soteriou C and Winterbourne M. Instantaneous and ensemble average cavitation structures in Diesel micro-channel flow orifices. Fuel. 2014; 116: 736-42.

49. Toro E. Riemann Solvers and Numerical Methods for Fluid Dynamics: A Practical Introduction. Springer-Verlag Berlin Heidelberg, 2009.

50. Koukouvinis P, Gavaises M, Georgoulas A and Marengo M. Compressible simulations of bubble dynamics with central-upwind schemes. International Journal of Computational Fluid Dynamics. 2016.